



**HAL**  
open science

## Measuring vertical velocities with ADCPs in low-energy ocean

Caroline Comby, Stéphanie Barrillon, Jean-Luc Fuda, Andrea M. Doglioli, Roxane Tzortzis, Gérald Grégori, Melilotus Thyssen, Anne Petrenko

► **To cite this version:**

Caroline Comby, Stéphanie Barrillon, Jean-Luc Fuda, Andrea M. Doglioli, Roxane Tzortzis, et al.. Measuring vertical velocities with ADCPs in low-energy ocean. *Journal of Atmospheric and Oceanic Technology*, 2022, 39 (11), pp.1669-1684. 10.1175/JTECH-D-21-0180.1 . hal-03746757v2

**HAL Id: hal-03746757**

**<https://amu.hal.science/hal-03746757v2>**

Submitted on 15 Oct 2024

**HAL** is a multi-disciplinary open access archive for the deposit and dissemination of scientific research documents, whether they are published or not. The documents may come from teaching and research institutions in France or abroad, or from public or private research centers.

L'archive ouverte pluridisciplinaire **HAL**, est destinée au dépôt et à la diffusion de documents scientifiques de niveau recherche, publiés ou non, émanant des établissements d'enseignement et de recherche français ou étrangers, des laboratoires publics ou privés.

Copyright

## Measuring Vertical Velocities with ADCPs in Low-Energy Ocean

CAROLINE COMBY,<sup>a</sup> STÉPHANIE BARRILLON,<sup>a</sup> JEAN-LUC FUDA,<sup>a</sup> ANDREA M. DOGLIOLI,<sup>a</sup> ROXANE TZORTZIS,<sup>a</sup>  
GÉRALD GRÉGORI,<sup>a</sup> MELILOTUS THYSSEN,<sup>a</sup> AND ANNE A. PETRENKO<sup>a</sup>

<sup>a</sup> Aix Marseille Univ., Université de Toulon, CNRS, IRD, MIO UM 110, Marseille, France

(Manuscript received 4 January 2022, in final form 17 May 2022)

**ABSTRACT:** Vertical velocities knowledge is essential to study fine-scale dynamics in the surface layers of the ocean and to understand their impact on biological production mechanisms. However, these vertical velocities have long been neglected, simply parameterized, or considered as not measurable, due mainly to their order of magnitude (less than  $\text{mm s}^{-1}$  up to  $\text{cm s}^{-1}$ ), generally much lower than the one of the horizontal velocities ( $\text{cm s}^{-1}$  to  $\text{dm s}^{-1}$ ), hence the challenge of their in situ measurement. In this paper, we present an upgraded method for direct in situ measurement of vertical velocities using data from different acoustic Doppler current profilers (ADCPs) associated with CTD probes, and we perform a comparative analysis of the results obtained by this method. The analyzed data were collected during the FUMSECK cruise, from three ADCPs: two Workhorse (conventional ADCPs), one lowered on a carousel and the other deployed in free-fall mode, and one Sentinel V (a new-generation ADCP with four classical beams and a fifth vertical beam), also lowered on a carousel. Our analyses provide profiles of vertical velocities on the order of  $\text{mm s}^{-1}$ , as expected, with standard deviations of a few  $\text{mm s}^{-1}$ . While the fifth beam of the Sentinel V exhibits a better accuracy than conventional ADCPs, the free-fall technique provides a more accurate measurement compared to the carousel technique. Finally, this innovative study opens up the possibility to perform simple and direct in situ measurements of vertical velocities, coupling the free-fall technique with a five-beam ADCP.

**KEYWORDS:** Ocean; Ageostrophic circulations; Vertical motion; Surface layer; In situ oceanic observations

### 1. Introduction

The study of the oceanic vertical velocities arises increasing interest in the oceanographic community. Numerous studies are conducted in high-energy ocean regions, with estimation of large vertical motions. Vertical velocities are generally estimated by the omega equation, hereinafter noted  $\omega$  equation (Tintoré et al. 1991; Pollard and Regier 1992; Fiekas et al. 1994; Strass 1994; Pinot et al. 1996; Shearman et al. 1999; Allen et al. 2001; Giordani et al. 2006; Canuto and Cheng 2017). According to these studies, performed in high-energy circulation areas (California Current System, Alboran Sea, northeast Atlantic during the winter season, etc.), the authors report vertical velocities of  $4\text{--}40 \text{ m day}^{-1}$  ( $\approx 10^{-5}\text{--}10^{-4} \text{ m s}^{-1}$ ). Yu et al. (2019) used the nondiffusive density equation for measurements at fixed moorings and estimated submesoscale vertical velocities of  $38.0 \pm 6.9 \text{ m day}^{-1}$  ( $\approx 10^{-4} \text{ m s}^{-1}$ ). Lindstrom and Watts (1994) used, among others comparative methods, the heat equation and thermal wind imbalance combining temperature and current measurements. On the eastern boundary of the Gulf Stream, these authors estimated vertical velocities reaching values of  $1\text{--}2 \times 10^{-3} \text{ m s}^{-1}$ , with rare values up to  $3 \times 10^{-3} \text{ m s}^{-1}$ .

Bower and Rossby (1989), Lindstrom and Watts (1994), Steffen and D'Asaro (2002), and D'Asaro et al. (2017) directly integrate vertical displacement measurements of their Lagrangian drifters, and obtain vertical velocities ranging from  $10^{-3}$  to  $10^{-2} \text{ m s}^{-1}$ . Merkelbach et al. (2010), Frajka-Williams

et al. (2011), Fuda et al. (2013), and Margirier et al. (2017) analyze the vertical velocity anomalies of gliders with respect to their flight models. According to these studies, the authors determine average vertical velocities of  $1\text{--}6 \times 10^{-2} \text{ m s}^{-1}$ . For rare deep convection events, oceanic vertical velocities reach  $0.1 \text{ m s}^{-1}$  according to Merkelbach et al. (2010) and  $0.18 \text{ m s}^{-1}$  according to Margirier et al. (2017). These techniques, based on the vertical displacement integration of immersed instruments, are not widely spread but enable to state vertical velocities ranging from  $10^{-3}$  to  $10^{-1} \text{ m s}^{-1}$ .

Direct in situ measurement of vertical velocities with current meters is rather limited in the literature (Thurnherr 2011; D'Asaro et al. 2017; Tarry et al. 2021). For local studies in regions with strong vertical displacements, vertical velocities are quite well characterized [e.g., deep winter convection in Schott and Leaman (1991), and Schott et al. (1996)  $\approx 0.05\text{--}0.1 \text{ m s}^{-1}$ , or strong internal waves in Lien et al. (2005) up to  $0.2 \text{ m s}^{-1}$ ]. However, for low-energy ocean regions, representing the majority of the global ocean, direct in situ measurement of vertical velocities is still currently one of the biggest challenges in physical oceanography.

In this study, we estimate vertical velocities based on a method suitable for a low-energy region characterized by finescale structures, where we expected a magnitude of few  $\text{mm s}^{-1}$ . The fine scales, grouping the meso- and submesoscales, are characterized by typical spatiotemporal scales: a horizontal spatial scale ranging from 1 to 100 km, a vertical spatial scale which can extend from 0.1 to 1 km deep (Thomas et al. 2008; McWilliams 2016; Ruiz et al. 2019), as well as a lifetime ranging from a few days to a few weeks for the physical and biological processes generated in these structures

Corresponding author: Caroline Comby, caroline.comby@mio.osupytheas.fr

DOI: 10.1175/JTECH-D-21-0180.1

© 2022 American Meteorological Society. For information regarding reuse of this content and general copyright information, consult the AMS Copyright Policy ([www.ametsoc.org/PUBSReuseLicenses](http://www.ametsoc.org/PUBSReuseLicenses)).

(Giordani et al. 2006; Ferrari and Wunsch 2009). In addition, a Rossby number close to one ( $Ro \approx 1$ ) is typical of fine-scale processes and involves an oceanic circulation which deviates from geostrophic balance with the emergence of vertical velocities (Klein and Lapeyre 2009; Mahadevan and Tandon 2006; Sasaki et al. 2014). The general interest in fine scale and, more precisely, in the determination of vertical velocities, is explained by their key role in global oceanic balance and their impact on the vertical transfer of nutrients and carbon budget despite their low intensity (Martin et al. 2001; Lévy et al. 2012; Mahadevan 2016; McGillicuddy 2016; Lévy et al. 2018; Rousselet et al. 2019; Boyd et al. 2019). With the increasing global warming issues linked to the forcing of the carbon cycle by anthropogenic activities, the estimation of vertical velocities becomes an essential information for a better representation of biogeochemical budgets.

The French–American Surface and Water Ocean Topography (SWOT) mission will enable very high spatiotemporal resolution altimetry measurements, opening up the possibility of evaluating vertical velocity by satellite. These SWOT-derived vertical velocities will have to be compared with in situ measurements. Hence, in the framework of BioSWOT, a component of the SWOT project, we aim at developing dedicated instruments and methodologies for vertical velocity measurement. BioSWOT main objective is to study the fine-scale coupling between physics and biology. The Mediterranean Institute of Oceanography has already been principal investigator of two short BioSWOT cruises (2015, 2019). In 2015, during the Observing Submesoscale Coupling At High Resolution (OSCAHR) cruise (Doglioli 2015), we studied a fine-scale structure located in the Ligurian Sea (northeast of the western Mediterranean Sea) and found a link between biology and vertical velocities obtained with the  $\omega$  equation (Rousselet et al. 2019).

The present study was performed in the framework of the Facilities for Updating the Mediterranean Submesoscale–Ecosystem Coupling Knowledge (FUMSECK) cruise (Barrillon 2019), back in this same study area. One of the main objectives of this second cruise, carried out during spring 2019 in the Ligurian Sea, was to directly measure the vertical component of the current in the ocean surface layer by deploying classical instruments as well as new prototypes.

The different datasets acquired during the FUMSECK cruise aim at obtaining a direct in situ measurement based on four different methods using three acoustic Doppler current profilers (ADCPs): two classic Workhorse and one Sentinel V (next-generation ADCP providing two types of vertical velocity measurements), and ultimately, comparing the four methods.

The paper is structured as follows. In section 2, after a general description of the sampling methodology, we present a single, upgraded, and generalized method for processing acoustic data to obtain vertical velocities. In section 3, we analyze the ADCPs measurements acquired with the four different methods mentioned above. Following the discussion of these results (section 4), the main outcome of this work is to recommend a platform, which measurement sensitivity is sufficient to measure vertical velocities on the order of several

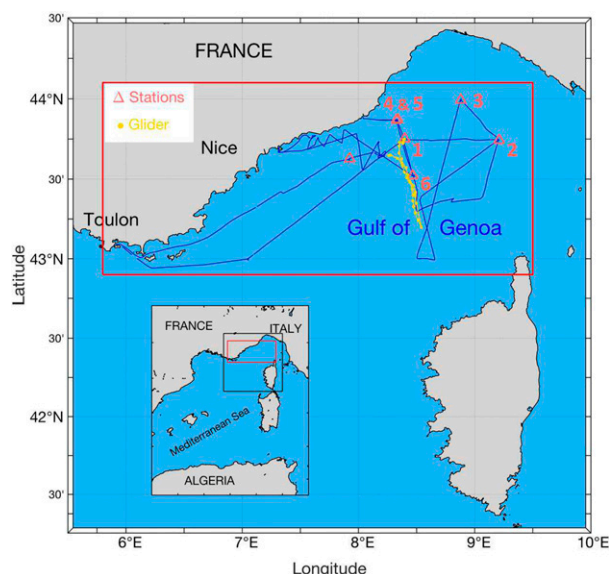


FIG. 1. Positioning of the vertical velocity stations (in orange, with their numbers) and roundtrip transect of the SeaExplorer glider (yellow dots). These data are superimposed on the route traveled by the oceanographic vessel *Tethys II* during the FUMSECK cruise (blue).

$10^{-3}$  to  $10^{-2}$   $m s^{-1}$ . To establish a solid foundation for the study, we also provide a detailed analysis of the potential sources of error in the measurements.

## 2. Data and methods

### a. Sampling methodology

The FUMSECK cruise took place from 30 April to 7 May 2019, in the Ligurian Sea, between latitudes 43° and 44°N and longitudes 7° and 10°E (Fig. 1). Three ADCPs, developed by Teledyne RD Instrument, were used in situ during this study: (i) two Workhorse 300 kHz (ADCP with the standard four beams), deployed according to one method each (either lowered from the CTD–ADCP package on a carousel, or dropped in free-fall), and (ii) one Sentinel V 500 kHz (ADCP with a vertical fifth beam to measure directly the vertical component of the current, in addition to the four conventional beams).

To simplify the reading thereafter, we will use the following terms to distinguish both the instruments and their use:

- L-ADCP, corresponding to the lowered Workhorse;
- L-V4, corresponding to the measurements from the four conventional beams of the lowered Sentinel V;
- L-V5th, corresponding to the measurements from the fifth beam (vertical beam) of the same lowered Sentinel V;
- FF-ADCP, corresponding to the free-falling Workhorse.

The L-ADCP and the Sentinel V were fixed under a Sea-Bird SBE 911 + conductivity–temperature–depth (CTD) probe (acquisition frequency at 24 Hz), and used, only one ADCP at a time, to perform profiles within the first 150 m of

the water column at six chosen stations. The two types of ADCPs have the same data sampling frequency of 1 Hz. The FF-ADCP was associated with a RBR concerto CTD probe (<https://rbr-global.com/products/standard-loggers/rbrduo-ct>) which sampling frequency was set to correspond to the one of the Workhorse ADCP (1 Hz). In addition, all the instruments have been parameterized to perform vertical velocity measurements in 5-m-thick cells.

Note that the locations of the stations were decided in order to grid the study area by carrying out butterfly-shaped transects, as shown in Fig. 1. Moreover, the positioning of the stations was chosen to sample a variety of situations, in a region characterized by a low-energy cyclonic recirculation (Astraldi et al. 1990; Millot 1999; Rousselet et al. 2019), bounded by a coastal southwestward current (the Northern Current) (Millot 1999; Petrenko 2003; Meloni et al. 2019).

The station measurements were performed first with an immersion of the CTD–ADCP package (Fig. 2a) at a fixed depth (about 10 m) for 10 min, followed by three successive vertical profiles between the surface and 150 m. This sampling technique has been used for several decades to establish vertical profiles of horizontal currents (Weller et al. 1990; Firing and Gordon 1990; Fischer and Visbeck 1993; Polzin et al. 2002), but has only rarely been applied specifically for the measurement of vertical velocities (Thurnherr 2011). To avoid any acoustic interference between the two lowered instruments, the L-ADCP and the Sentinel V were used alternately on each of the stations during the cruise.

After these measurements, series of three to five profiles were performed with the ADCP dropped in free-fall (FF-ADCP). The FF-ADCP, also associated with a CTD probe (Fig. 2b), was connected to the ship by a simple rope with enough slack to allow the package to fall freely in the water column, before being raised back to the ocean surface thanks to the rope.

Note that the first station (station 1) was not sampled with the FF-ADCP, and one other station (station 4) was sampled only with the Sentinel V and the FF-ADCP, due to a swell that was too strong to carry out safely the second sampling with the L-ADCP.

### b. Conventional 4 beams ADCP dataset processing

When the ADCP is submerged in the water column, its orientation is free to deviate from the gravimetric vertical direction due to several forces applied to the CTD–ADCP package. In particular, when the instruments are connected to the boat by the electric carrier cable, the restoring force of the boat, as well as the forces due to the horizontal currents and the swell, are acting on the package, in addition to its weight. All these forces acting on the instrument package cause deviations relative to the gravimetric vertical direction that must be taken into account when processing data from the ADCPs. Otherwise, they cause errors in the vertical velocity computation. The analysis chain described below corrects for these anomalies, subtracts the instrument vertical velocity, and synchronizes it with the CTD data.

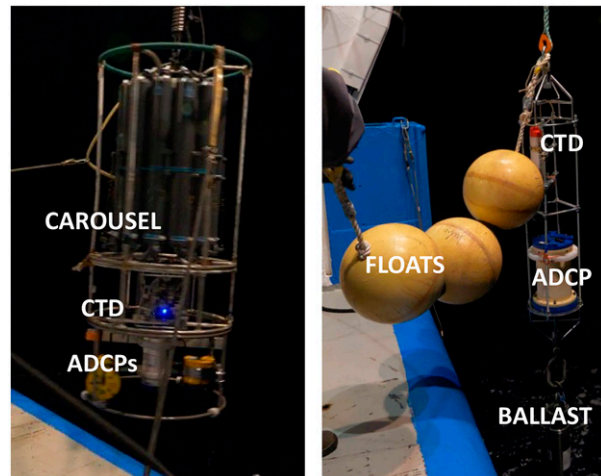


FIG. 2. ADCP deployment configuration for (left) the lowered technique and (right) the free-fall technique.

### 1) STEPS 0 AND 1: PREPARATION OF DATASETS

Before performing any processing on the measurements, preliminary steps are performed.

Indeed, the analysis method involving two sets of data (CTD and ADCP data), it is essential to synchronize these two sequences (step 0).

To do so, if the data acquisition by the CTD probe is made at a higher frequency than the one made by the ADCP (e.g., CTD Sea-Bird at 24 Hz versus Workhorse and Sentinel V at 1 Hz), a time smoothing over a period similar to the acquisition rate of the ADCP (here 1 Hz) is applied to the CTD sequence.

Following this optional smoothing, the CTD and ADCP sequences are systematically synchronized in time with the following method: (i) the distribution of the pressure differences between the two datasets is evaluated as a function of a time offset imposed on one of the sequences, (ii) the synchronization is considered optimal when the standard deviation of this distribution is minimal. Great attention is paid to possible data gaps in each instrument time series, which would induce the desynchronization of the subsequent data.

Then, according to different quality criteria, a data selection is applied in order to discard potentially erroneous measurements (step 1). These quality criteria are based on the following:

- A retrodiffused echo intensity greater than 40 counts. This inferior limit is fixed by the instrument manufacturer RDI. The counts represent a linear scale on which retrodiffused echo intensity is encoded, and the threshold of 40 counts equals about 16% of emitted signal intensity.
- A correlation between the emitted and retrodiffused signal greater than 64 counts. This inferior limit is fixed by the instrument manufacturer RDI. Here, the counts represent a linear scale on which signals correlation is encoded, and the threshold of 64 counts equals about 25% of correlation. This correlation threshold also makes it possible to locate

TABLE 1. Characteristics of the pressure sensors.

	Sensor				
	SBE 911	RBR concerto	Sentinel V50	Workhorse 300	Workhorse 300
Technique	Lowered	Free-fall	L-V4 and L-V5	L-ADCP	FF-ADCP
Full scale (m)	6800	750	300	6000	200
Accuracy (m)	1.02	0.365	0.3	15	0.5
Resolution (cm)	6.8	0.75	0.1	15	0.5

possible recordings of acoustic interference by punctual decreases in the correlation value. In the presence of acoustic interference, their estimated constant velocity propagation in the recordings is used to easily isolate them from the rest of the vertical velocity recordings and then remove them by NaN flag.

- An absolute error velocity lower than  $0.1 \text{ m s}^{-1}$ . Two vertical velocity estimates being calculated by the two pairs of opposed beams, the error velocity represents the difference between the two estimates.

## 2) STEP 2: REFERENCE FRAME TRANSFORMATION AND DEPTH VECTOR PROJECTION

As mentioned above, when the ADCP is immersed in the water column, its vertical axis is free to deviate from the gravimetric vertical direction. The magnetic compass integrated in the ADCP makes it possible to determine the orientation of the instrument in the water column. This orientation is characterized by three attitude angles, also called gimbal angles: pitch ( $\theta_P$ ), roll ( $\theta_R$ ), and heading ( $\theta_H$ ).

The recording of vertical velocities by the four beams having been configured in Earth coordinates ( $w_t$ , terrestrial reference frame), these data must be associated with the appropriate depths in the same reference frame. To obtain the Earth coordinates of the depth vector ( $x_t, y_t, z_t$ ), the principle is to project the tilted ADCP acoustic cell [(0, 0,  $z_s$ ) in the ADCP reference frame] on the vertical axis, using the attitude angles as shown in the following equation:

$$z_t = \cos \theta_P \times \cos \theta_R \times z_s. \quad (1)$$

## 3) STEP 3: ABSOLUTE VERTICAL VELOCITIES

Once the depth has been projected, the oceanic vertical velocity is calculated in the water column ( $w$ ). For this step, we consider that the measurement of the vertical component of the velocity, given by the ADCP configuration in Earth coordinates ( $w_t$ , zenith-oriented vertical axis), is the result of two vertical components, expressed in the same frame of reference (also zenith-oriented vertical axis):

- the vertical velocity  $w$  of the oceanic current in the water column;
- the vertical velocity of the instruments package  $w_{\text{pkg}}$  calculated from the hydrostatic approximation, considering

$$w_{\text{pkg}} = -\frac{1}{\rho g} \frac{\partial p}{\partial t}, \quad (2)$$

where  $p$  is pressure,  $\rho$  is density, and  $g$  is the gravitational acceleration constant.

The dynamic pressure, resulting from the instrument vertical velocity estimated at  $1 \text{ m s}^{-1}$  in the lowered method and  $0.3 \text{ m s}^{-1}$  in the free-fall method, reaches, respectively, 500 and 50 Pa, representing an error on the depth estimation of about 5 and 0.5 cm, which is below the accuracy of the pressure sensors (see Table 1). This justifies the use of the hydrostatic hypothesis in this study.

Each ADCP has its own pressure sensor, and each of the sampling methods (lowered and free-fall) is associated with a CTD probe (SBE 911 and RBR concerto, respectively) to ensure a second pressure measurement. The characteristics of all the pressure sensors used in the study are presented in Table 1. The accuracy of the pressure data is a very important constraint on estimating the instrument vertical velocity.

For the estimation of the Sentinel V vertical velocity, we directly use the data from its internal pressure sensor. Indeed, this sensor is much more accurate and has a better resolution than the CTD probe (SBE 911), due to its smaller full scale.

Our SBE 911 probe is adapted to measurements reaching 6800 m. Thus, for measurements limited to the first 200 m, this pressure sensor is no longer well suited. However, we performed a calibration of the SBE pressure dataset using the corresponding Sentinel V pressure dataset. To do this, we performed a linear regression between the Sentinel V and SBE pressure records for each sampling phase (fixed at 10 m, downcast, upcast). These coefficients barely fluctuate between stations, hence the use of average coefficients calculated for all the stations. These regression coefficients are then applied to the SBE pressure data recorded in the corresponding sampling phases, to obtain calibrated pressure data. We validate this calibration by the excellent agreement between the final ocean vertical velocity profiles using calibrated SBE and Sentinel V pressure data.

For the L-ADCP method, the pressure sensor associated with the Workhorse is dedicated to sampling as deep as the SBE, and far beyond the sampling range of our study. For this reason, we use the calibrated SBE pressure data for the L-ADCP fall rate estimation.

Finally, for the FF-ADCP method, the use of the CTD pressure sensor (RBR concerto) provides the more accurate estimation of the instrument velocity.

Thereafter, the vertical oceanic velocity is obtained from

$$w = w_t + w_{\text{pkg}}. \quad (3)$$

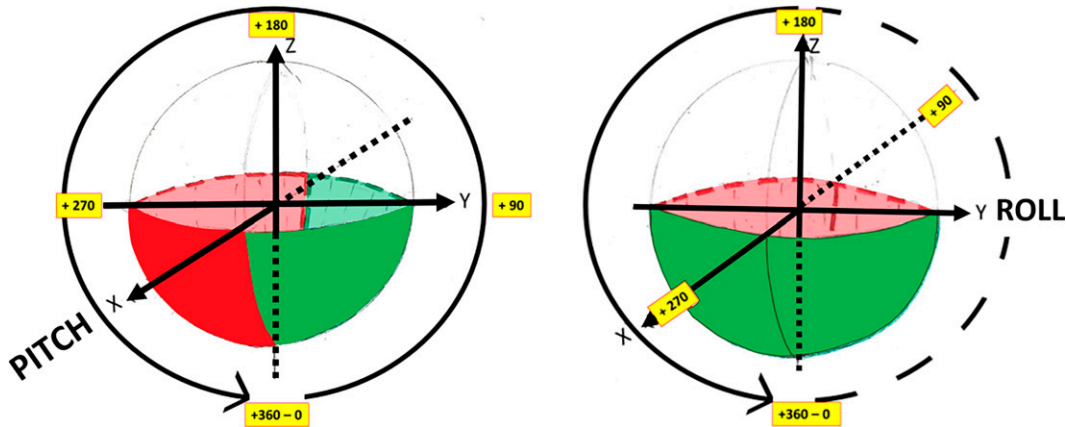


FIG. 3. Schemes of spherical conventions for (left) pitch and (right) roll data.

#### 4) STEPS 4 AND 5: TEMPORAL SMOOTHING AND FINAL VERTICAL PROFILES

Two final steps are applied in this data processing chain.

The measurements recorded at the ADCP rate (one measurement by “ping,” every second) are usually showing a high standard deviation. Thus, a temporal smoothing over an optimized window of 20 s is applied and reduces the uncertainties of the measurement caused by isotropic turbulence and background noise.

Finally, due to this statistical approach, a cut at the upper and lower ends of the vertical profiles of  $w$  is applied, to overcome the potential bias linked to a much smaller data occurrence at these ends. Indeed, the “yo-yo” cast between the top and the bottom of the profile being recorded at approximately  $1 \text{ m s}^{-1}$  with the lowered method and  $0.3 \text{ m s}^{-1}$  with the free-fall method, the body of the profile is sampled a great number of times during the downward/upward movement due to the range of the ADCP used (between 30 and 80 m). Therefore, there is a higher number of measurement occurrences in the thickness defined by the range of the instrument when the ADCP data overlap compared to the two ends of the profiles.

Hence, we have eliminated the first four bins of the ADCP close to the surface, where the measurements are the most affected by noise, leading to the beginning of the profile at 25 m depth. At the bottom of the profiles, we define the cut-off depth as the minimal level reached by the instrument among the downcast phases, for each corresponding station. Note that in the case of FF-ADCP, dropped at about 80 m depth instead of 150 m depth, the lower cutoff depth is chosen at the minimum depth among the downcast phases where the vertical velocity data start to be cut by the correlation criteria (step 1).

#### c. New fifth beam ADCP dataset processing

As mentioned above, forces acting on the instrument and causing deviations relative to the gravimetric vertical direction must be taken into account, especially when processing data from the fifth beam (in the main axis of the instrument) of the Sentinel V. Indeed, the measurements from the fifth beam, expressed in the instrument reference frame, are

directly affected by these forces and cause major vertical velocity anomalies on recordings. To correct the measurement from this fifth beam, we use the processing chain described above and add two specific steps, as follows.

#### 1) STEP 2A: ADCP ATTITUDE ANGLES AND GENERALIZATION IN SPHERICAL CONVENTION

The values of the attitude angles (pitch, roll and heading) measured by the Teledyne RD Instruments (Sentinel V) follow a convention based on intervals between  $0^\circ$  and  $\pm 90^\circ$ . Such a convention, initially adopted for deployments with fixed mooring, is not optimal for widespread use of vertical profiles in the water column. Indeed, with this convention, the direction of the beams of the instrument (toward the surface or the bottom) cannot be distinguished, which implies adapting the measurement reference system for each use.

This is why we carry out the generalization of the angles in spherical convention, characterized by angular intervals ranging between  $0^\circ$  and  $360^\circ$ , as shown in Fig. 3. This spherical convention is much more conducive for data processing: on one hand, it eliminates the need to adapt the measurement reference system for each use of the Sentinel V, and on the other hand, it is applicable to all types of measurements made by other ADCPs based on various conventions.

#### 2) STEP 2B: REFERENCE FRAME TRANSFORMATION AND CORRECTIONS BY PROJECTION

When the orientation of the Sentinel V deviates from the gravimetric vertical direction, the fifth beam of the ADCP records a signal resulting from different proportions of both horizontal and vertical components of the current. This effect is enhanced by the significantly different orders of magnitude between these three components: on the order of  $10^{-2}$ – $10^{-1} \text{ m s}^{-1}$  for the two horizontal components, and on the order of  $10^{-3}$ – $10^{-2} \text{ m s}^{-1}$  for the vertical component. To obtain only the vertical component of the current, it is therefore necessary to correct the measurement of the fifth beam of the ADCP. This correction is determined by the use of the rotation matrices which project any vector measured in one given reference

frame to another. Here, the use of rotations around the axes of Sentinel V, listed below (with the angles having been set in spherical convention), makes it possible to project any vector initially expressed in the reference frame of the instrument (orthonormal basis composed by beams 1–2, beams 3–4, and beam 5 axes) toward the Earth coordinates (orthonormal basis composed by east, north, and zenith axes):

- heading (**H**, clockwise rotation around the axis of the vertical beam—beam 5);
- pitch (**P**, trigonometric rotation around the *X* axis—beam 1 to beam 2);
- roll (**R**, trigonometric rotation around the *Y* axis—beam 3 to beam 4).

Here we use the rotation matrices to project any vector in Earth coordinates. The rotations must be applied successively, with the rotation signs as follows: first **R**, then **-P**, and finally **H**, corresponding to  $\mathbf{H} \cdot -\mathbf{P} \cdot \mathbf{R}$  as shown by the matrix product below:

$$\mathbf{M} = \begin{bmatrix} \cos \theta_H & \sin \theta_H & 0 \\ -\sin \theta_H & \cos \theta_H & 0 \\ 0 & 0 & 1 \end{bmatrix} \begin{bmatrix} 1 & 0 & 0 \\ 0 & \cos \theta_P & -\sin \theta_P \\ 0 & \sin \theta_P & \cos \theta_P \end{bmatrix} \times \begin{bmatrix} \cos \theta_R & 0 & -\sin \theta_R \\ 0 & 1 & 0 \\ \sin \theta_R & 0 & \cos \theta_R \end{bmatrix}, \tag{4}$$

$$\Leftrightarrow \mathbf{M} = \begin{bmatrix} \cos \theta_H \cos \theta_R - \sin \theta_H \sin \theta_P \sin \theta_R & \sin \theta_H \cos \theta_P & -\cos \theta_H \sin \theta_R - \sin \theta_H \sin \theta_P \cos \theta_R \\ -\sin \theta_H \cos \theta_R - \cos \theta_H \sin \theta_P \sin \theta_R & \cos \theta_H \cos \theta_P & \sin \theta_H \sin \theta_R - \cos \theta_H \sin \theta_P \cos \theta_R \\ \cos \theta_P \sin \theta_R & \sin \theta_P & \cos \theta_P \cos \theta_R \end{bmatrix}. \tag{5}$$

**M** is applied to the components of the velocity measured in the reference frame of the Sentinel V ( $u_s, v_s, w_s$ ) to obtain these same components in Earth coordinates ( $u_t, v_t, w_t$ ), according to the following formula:

$$\begin{bmatrix} u_t \\ v_t \\ w_t \end{bmatrix} = \mathbf{M} \cdot \begin{bmatrix} u_s \\ v_s \\ w_s \end{bmatrix}. \tag{6}$$

From the measurements of the components  $u_t$  and  $v_t$ , obtained from the four beams, as well as the component  $w_s$  from the fifth beam, and knowing that this passage matrix is invertible, we can calculate the vertical component of the current in Earth coordinates ( $w_t$ ) according to

$$w_t = \frac{w_s + u_t(\cos \theta_H \sin \theta_R + \sin \theta_H \sin \theta_P \cos \theta_R) + v_t(-\sin \theta_H \sin \theta_R + \cos \theta_H \sin \theta_P \cos \theta_R)}{\cos \theta_R \cos \theta_P}. \tag{7}$$

Furthermore, it is important to note that this step of referential changes, specific to the velocity measurement acquired by the fifth beam of the Sentinel V, does not intervene in the data processing chain measured by the four beams of the Sentinel V and conventional ADCPs, if the data used are already in Earth coordinates.

In addition the depth projection of the acoustic cells in Earth coordinates, with the approximation of (0, 0,  $z_s$ ) and the application of **M**, leads to Eq. (1) and to what follows in the processing chain.

The effect of this processing chain on the data is illustrated in Fig. 4, showing the vertical velocity profiles before and after the application of the processing chain, for the example of station 6. In this example, after the analysis, the magnitude of the vertical velocity has diminished by an order of  $10^2$ , and the upcasts and downcasts records tend to match.

*d. Error propagation method*

Four sources of error, identified and estimated by the manufacturer of the ADCPs, relate to (i) the slope of the acoustic

tiles; (ii) the estimation of the tilts (pitch and roll); (iii) the estimation of the horizontal components ( $u$  and  $v$ ); and, in the specific case of the L-V5th measurements, (iv) the estimation of the vertical component ( $w_s$ ). A series of error propagation tests were performed on the vertical velocity measurements to highlight the contribution of each of the identified instrumental error sources in the estimation of oceanic vertical velocities.

Except for the first identified source, the tile slope, which is a constant error (set between  $-2^\circ$  and  $+2^\circ$  with  $0.5^\circ$  steps), all the other errors are characterized as random noise whose uncertainties are provided by the manufacturer. Each test was performed following the same principle. First, a uniform random subsampling of 100 oceanic vertical velocities measured in downcast phase by a given ADCP and for a given station is performed (noted  $w_{sub}$ ). Then, for each of these 100 subsamples, a random error is added, with a normal distribution centered on the value corresponding to the uncertainty provided by the manufacturer. Adding this noise is performed 500 times for each subsample, to obtain 100 artificial distributions (noted  $w'$ ) of statistically representative size ( $5 \times 10^4$  data per test).

To summarize, we have run five series of tests:

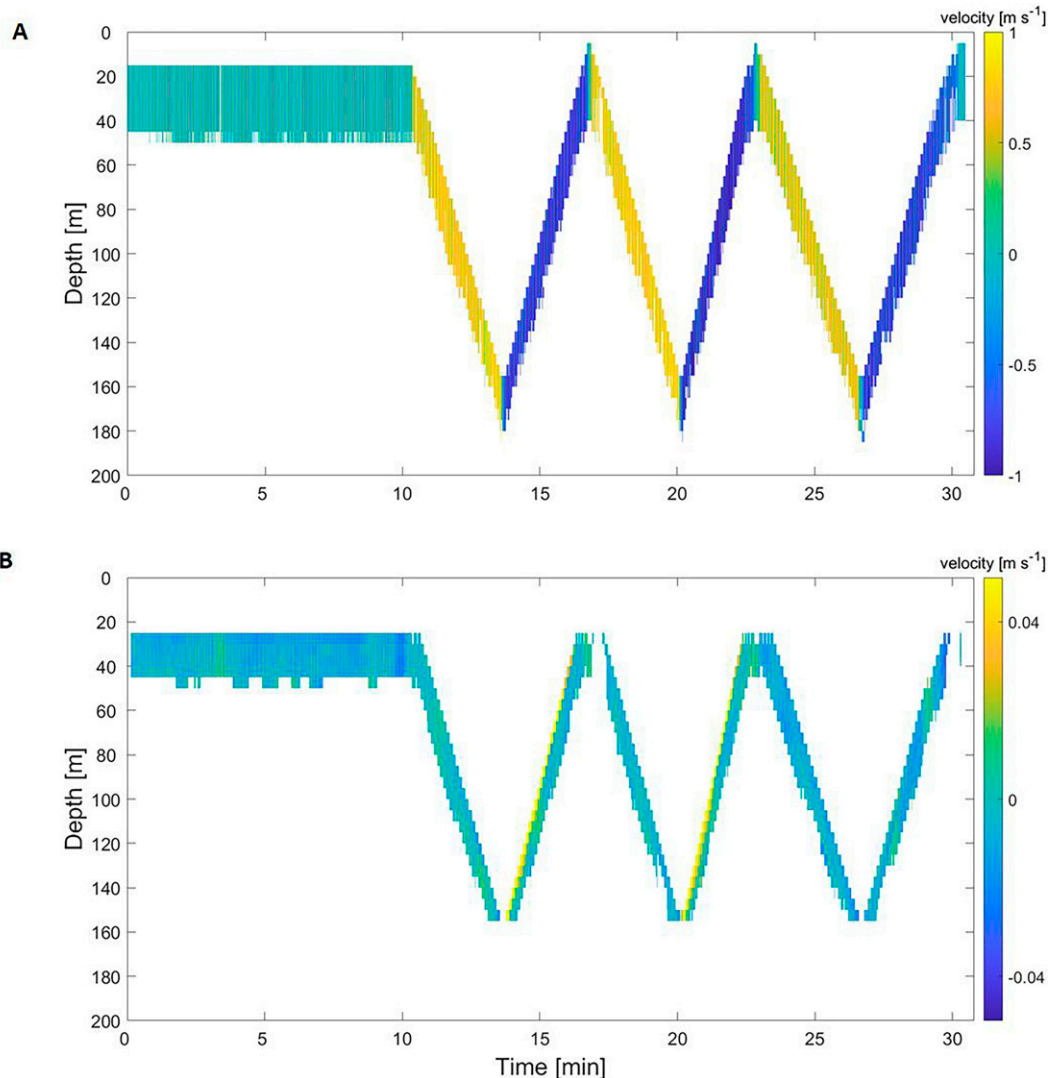


FIG. 4. Vertical velocities profiles measured by the fifth beam of Sentinel V (L-V5th) (a) before and (b) after the application of the processing chain displayed as a function of time and depth for in situ measurements at station 6 of the FUMSECK cruise.

- 1) Tile slope: A constant error on the inclination of the acoustic tile is added. This first series contains nine tests with fixed error values ranging from  $-2^\circ$  to  $+2^\circ$  with a step of  $0.5^\circ$ .
- 2) Pitch/roll: We add, to the tile slope test series, a random error on the pitch/roll measurement with a Gaussian distribution (accuracy  $0.05^\circ$ ).
- 3) Horizontal components  $u$  and  $v$ : We add, to the tile slope test series, a random error on the  $u/v$  measurement with a Gaussian distribution (accuracy  $3 \times 10^{-3} \text{ m s}^{-1}$ ).
- 4) Vertical component  $w_s$ : We add, to the tile slope test series, a random error on the  $w_s$  measurement with a Gaussian distribution (accuracy  $3 \times 10^{-3} \text{ m s}^{-1}$ ).
- 5) Combination of all error tests: We add, to the tile slope test series, the three random errors on the measurements presented above.

The results, presented in the dedicated section, correspond to the tests performed on the L-V5th measurements—station 1.

### 3. Results

#### a. Comparison of vertical velocity measurements obtained with the classic lowered method and the conventional four beams

The analysis chain, set up in section 2b to estimate vertical velocity measurements, is first applied on two datasets: (i) the four beams of the first Workhorse (classic L-ADCP), and (ii) those of the Sentinel V (L-V4), both provided by the processing software of these ADCPs. These measurements, recorded using the same deployment technique, are analyzed simultaneously in order to compare the two sets of results. Note that we use the standard deviation, defined as the square

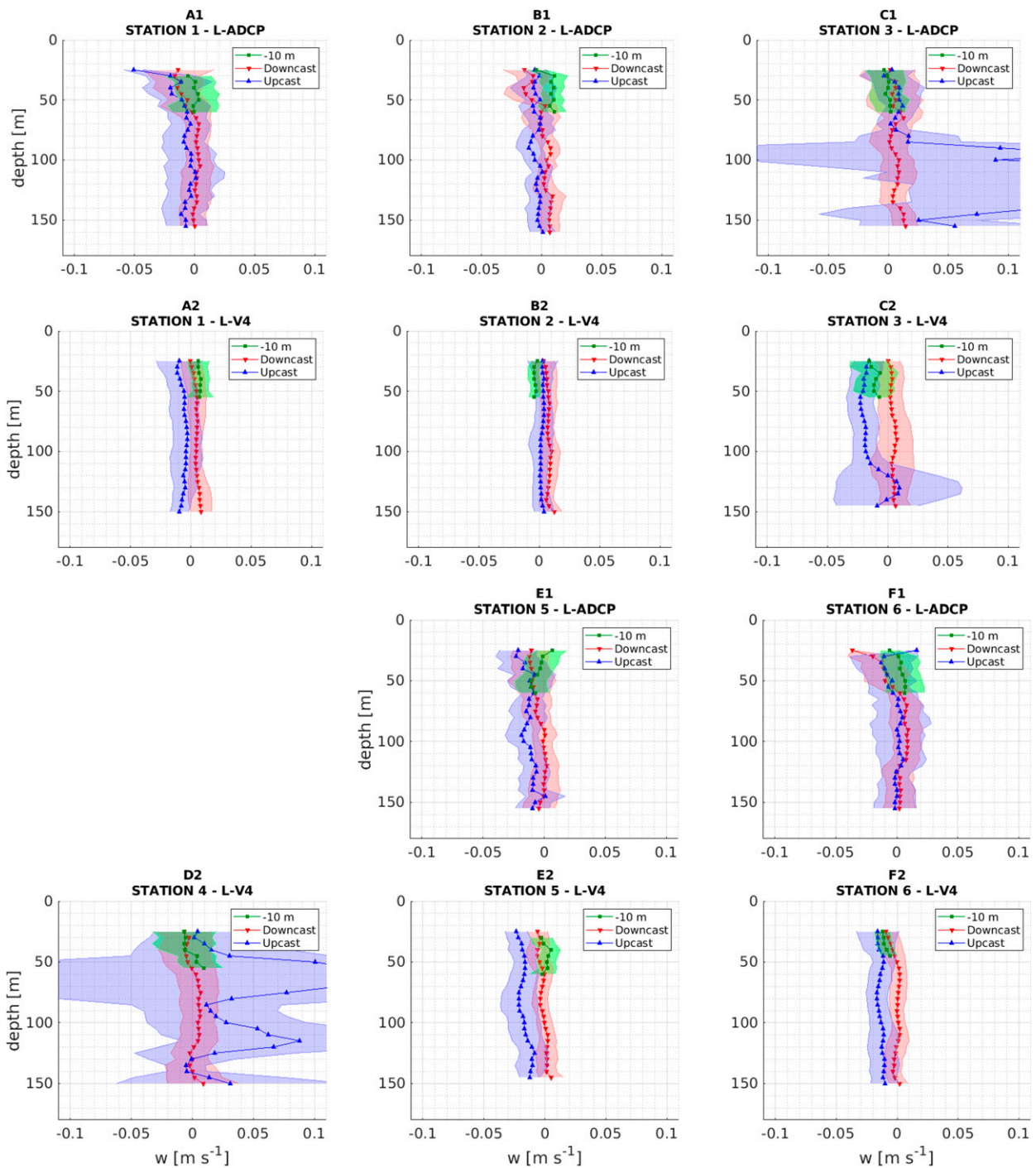


FIG. 5. Vertical velocities measured for stations 1 to 6 [(a1)–(f1)] by the classic L-ADCP and [(a2)–(f2)] by the L-V4. Means (lines and markers) and standard deviations (shaded areas) of vertical velocities are shown as a function of the depth for each of the acquisition phases: fixed at 10 m (green), downcast (red), and upcast (blue).

root of the sum of squared differences from the mean divided by the size of the dataset minus one, without considering the NaN values, in order to appreciate the variability of the measurements within each station.

Figure 5 shows the mean vertical profiles of the vertical velocities measured by the four beams of both the L-ADCP and the L-V4 in the CTD-ADCP package, for each station and differentiating the three acquisition phases: fixed immersion (at 10 m),

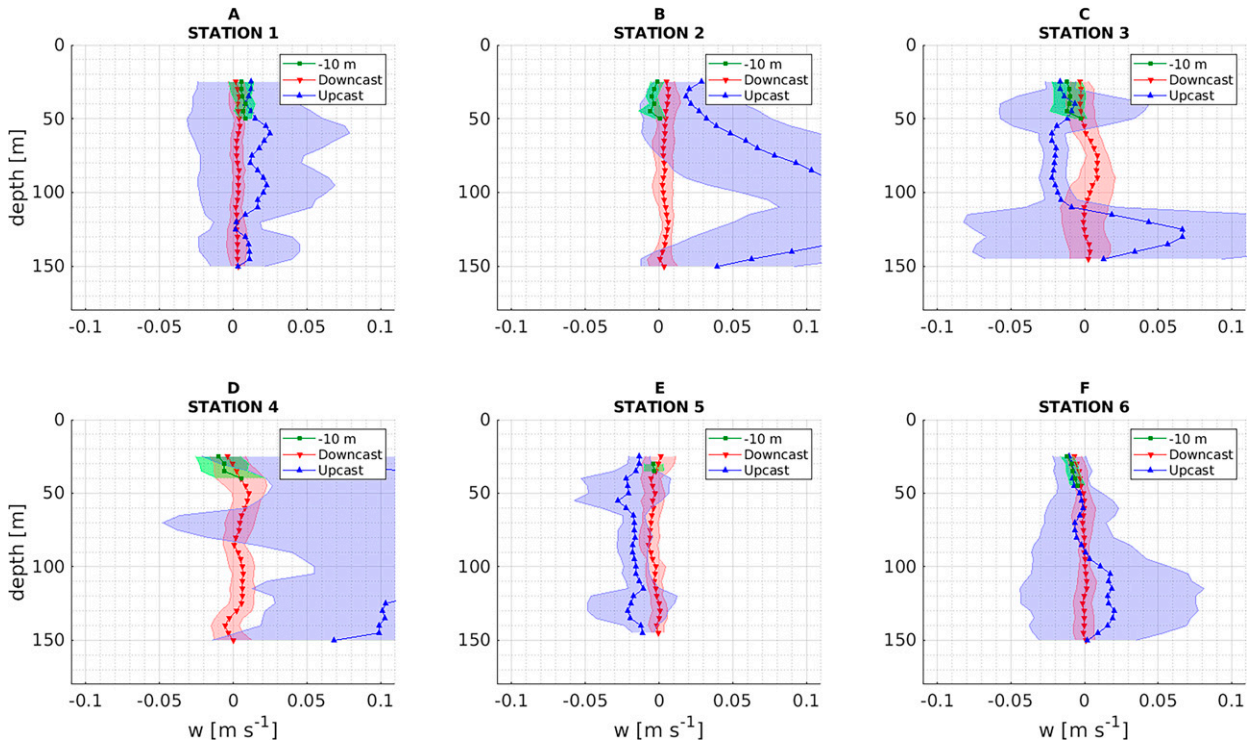


FIG. 6. Vertical velocities measured by the L-V5th for stations (a) 1 to (f) 6. Means (lines and markers) and standard deviations (shaded areas) of vertical velocities are shown as a function of the depth for each of the acquisition phases: fixed at 10 m (green), downcast (red), and upcast (blue).

downcasts, and upcasts. Station 4 was not sampled by the L-ADCP due to weather conditions unfavorable for the deployment. However, for the remaining stations, it is possible to compare the results from the two instruments lowered on the CTD-ADCP package.

Whatever the instrument, the whole analysis leads to a significant reduction in both the mean values (from 1 to  $10^{-3}$   $\text{m s}^{-1}$ ) and the standard deviations (from  $10^{-1}$  to  $10^{-2}$   $\text{m s}^{-1}$ ) of the vertical velocities, reaching the expected orders of magnitude.

We observe an agreement between the fixed immersion profiles and the downcast ones, while the upcast profiles are characterized by greater variability in the mean vertical velocity as a function of depth and by higher standard deviations. This specificity of upcast profiles probably results from two combined effects. On one hand, a vibration phenomenon of the wire cable connecting the CTD-ADCP package to the ship can disturb the measurements due to the cable tension which is more important during the upcasts. On the other hand, the ADCP ringing phenomenon, or resonance, seems to be more important during the upcasts for a reason still uncertain. Indeed, if the acoustic tile of an ADCP is still vibrating (or vibrating again) when a part of the outgoing acoustic signal, having backscattered on the marine particles near the tile, returns to that tile, this creates interference, called ringing or resonance effect. Usually, to avoid this bias, a blanking area—where the data are not taken into account—is applied in the immediate proximity of the tiles, allowing them to stop

vibrating before recording the return signals. In our case, this blanking zone seems insufficient during the upcasts. These combined effects were particularly visible at stations 3 and 4 (Fig. 5c1, 5c2, and 5d2), where we observe high values of positive velocities associated with large standard deviations on the upcasts. The sea state at station 4 was the worst of the cruise, but reasons of these effects at station 3 remain unknown. Hence, despite the good agreement of the recordings between the downcast and upcast phases on the other stations for the two ADCPs, the analysis of vertical velocities is subsequently carried out on the downcast profiles exclusively. This is a common method used for horizontal velocity measurements in vertical profiles by ADCPs (e.g., Polzin et al. 2002).

#### b. Vertical velocity measurements obtained with the classic lowered method and the new Sentinel V fifth beam

The results achieved by the analysis chain described above for the recordings of the L-V5th (section 2c) are presented in Fig. 6. This figure shows the profiles of the mean vertical velocity and its standard deviation, as in Fig. 5.

The results show profiles comparable to those of the conventional four beams. Here, the difference between downcast and upcast profiles is significant, for the same reasons as described in the previous section. The analysis of the downcast profiles highlights a low vertical variability of the mean vertical velocity. The orders of magnitude obtained by using the L-V5th

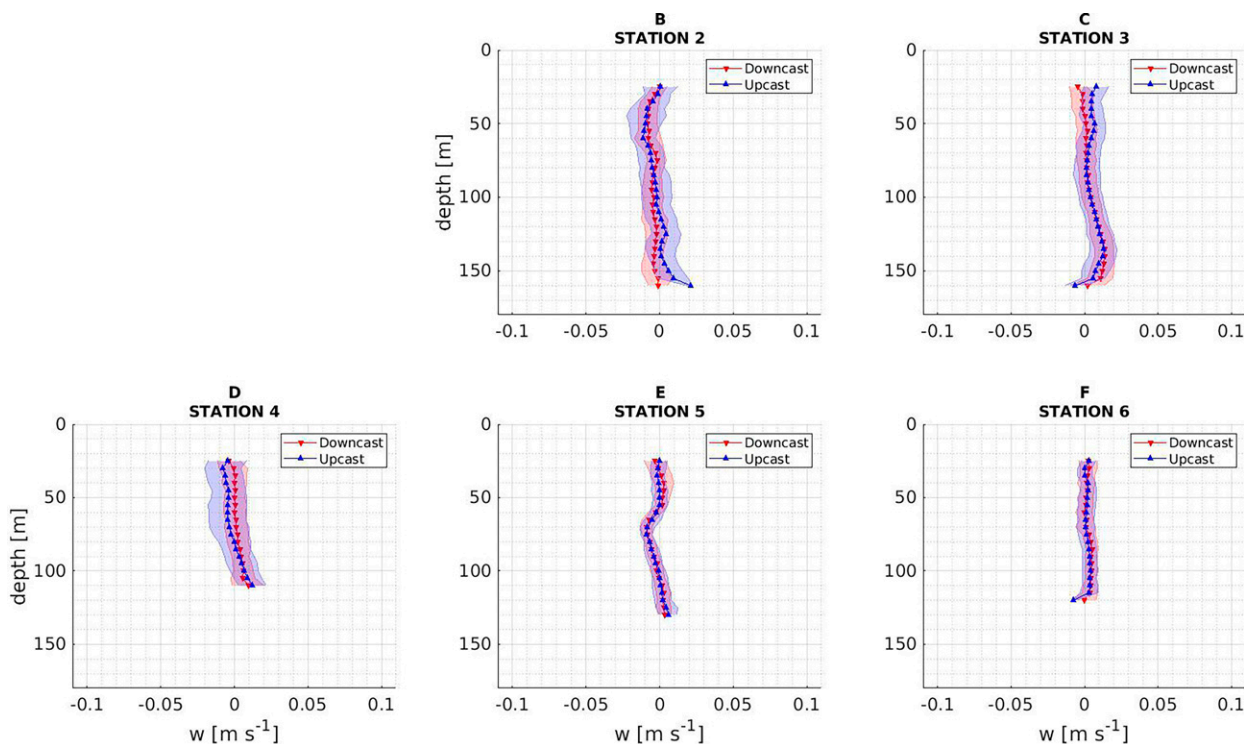


FIG. 7. Vertical velocities measured by the FF-ADCP for stations (b) 2 to (f) 6. Means (lines and markers) and standard deviations (shaded areas) of vertical velocities are shown as a function of the depth for each of the acquisition phases: downcast (red) and upcast (blue).

reach  $10^{-3} \text{ m s}^{-1}$  for means, and several  $10^{-3}$  to  $10^{-2} \text{ m s}^{-1}$  for standard deviations.

We note that the raw vertical velocity data, measured by the Sentinel V, have standard deviations on the order of several tens of  $10^{-2} \text{ m s}^{-1}$ , with an average on the order of  $1 \text{ m s}^{-1}$ , which corresponds to the recording of the predominant velocity component: the vertical movement of the instrument ( $w_{\text{CTD}}$ ). The estimate of the decrease in standard deviations following our data processing is approximately a factor of 20.

### c. Vertical velocity measurements obtained with the new free-fall method and the conventional four beams

In this last section, we applied our processing chain, described in section 2b, on the measurements performed by the second Workhorse deployed in free fall (FF-ADCP).

Figure 7 shows the vertical velocity profiles from the FF-ADCP differentiating the downcast and upcast phases according to the two previous figures. Here the means and standard deviations of downcast and upcast profiles match each other very well, which could be due to a greater stability of the ADCP caused by the use of a floating polypropylene rope rather than a wire cable. The free-falling technique provides great stability in the horizontal plane (pitch/roll variations) but foremost in the vertical axis. This limitation of vertical recalls is essential for the measurement of the vertical component of the current for which any disturbance in the same axis leads to the largest possible error. Despite this good

agreement, we focus on the profiles in the downcast phase only, to be coherent with the rest of the analysis.

All downcast profiles are rather homogeneous with respect to depth. The largest variation can be seen at station 5 (Fig. 7e), between 50 and 100 m depth, where the observed vertical velocity variation is statistically significant and corresponds to a negative vertical velocity signal (downward movement) in this part of the water column. This last analysis with our processing chain leads once again to measurements of average vertical velocities on the order of  $10^{-3} \text{ m s}^{-1}$  with standard deviations of several  $10^{-3} \text{ m s}^{-1}$ . Finally, it should be noted that these orders of magnitude, and more specifically that of the standard deviations, are systematically stable from one station to another.

### d. Error propagation results

After generating the artificial distributions, we studied the standard deviation produced by each test (Fig. 8) for the L-V5th data. First, we notice that the variation of the tile slope has no effect on the standard deviation, as expected. Second, for the tests on the pitch/roll and horizontal velocities, the standard deviations generated by the error sources at the end of the processing are less than  $10^{-4} \text{ m s}^{-1}$ , therefore largely negligible. Third, the error in the measurement of the vertical component ( $w_s$ ) generates a standard deviation on the order of  $10^{-3} \text{ m s}^{-1}$ . Among all the identified error sources, this latter contributes to most (over 99%) of the standard deviation generated by the error propagation test.

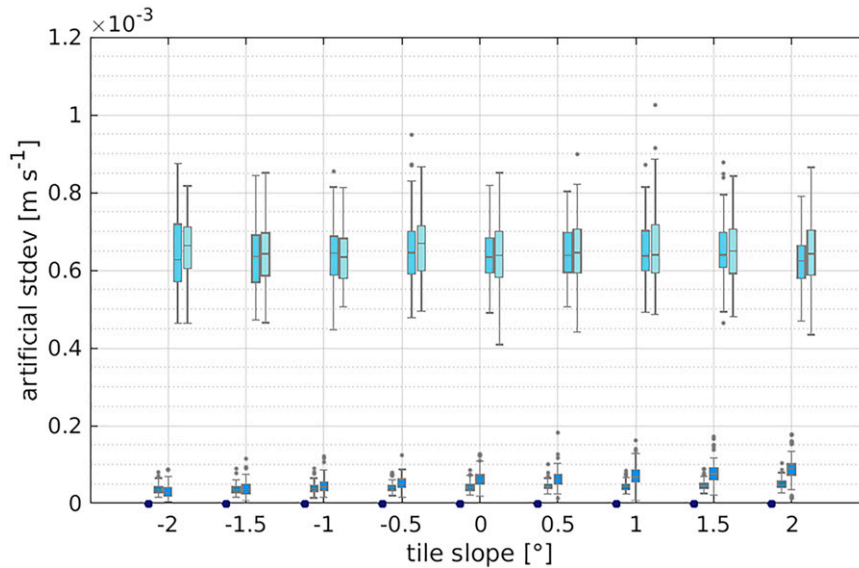


FIG. 8. Standard deviations presented for each error propagation test on tile slope, pitch/roll, horizontal velocities, vertical component  $w_s$ , and combined errors (from dark blue to light blue, respectively).

In summary, among the tests performed, the measurement error on the vertical component ( $w_s$ ) is the only identified source of error leading to an increase in the standard deviation at the end of the treatment. However, this source of error remains an order of magnitude smaller than the standard deviation observed in the final vertical velocity profiles.

For the tests on the tile slope, we found, beyond a negligible difference in standard deviation, a bias between the subsamples ( $w_{\text{sub}}$ ) and the artificial distribution mean generated from the subsamples ( $w'$ ).

The comparison of these biases with boxplot (Fig. 9) suggests that the greater the tile slope, the greater the bias, as expected, but also the greater the standard deviation of these biases. Yet it must be noted that only the variation of the tile slope causes this bias. Indeed, for the same tile slope there is no significant difference between the different tests. The information  $\pm 2^\circ$  indicated by RDI results in biases of up to  $\pm 2 \text{ cm s}^{-1}$ . Considering that standard deviations of up to  $1 \text{ cm s}^{-1}$  are observed, we assume that this error on the tile slope is below  $\pm 1^\circ$ .

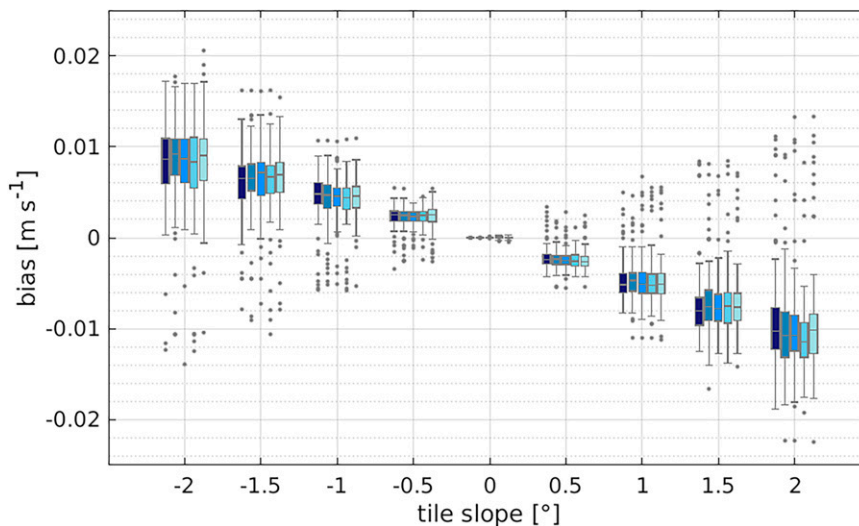


FIG. 9. Biases generated by each error propagation test on tile slope, pitch/roll, horizontal velocities, vertical component  $w_s$ , and combined errors (from dark blue to light blue, respectively), with  $\text{bias} = w_{\text{sub}} - w'$ .

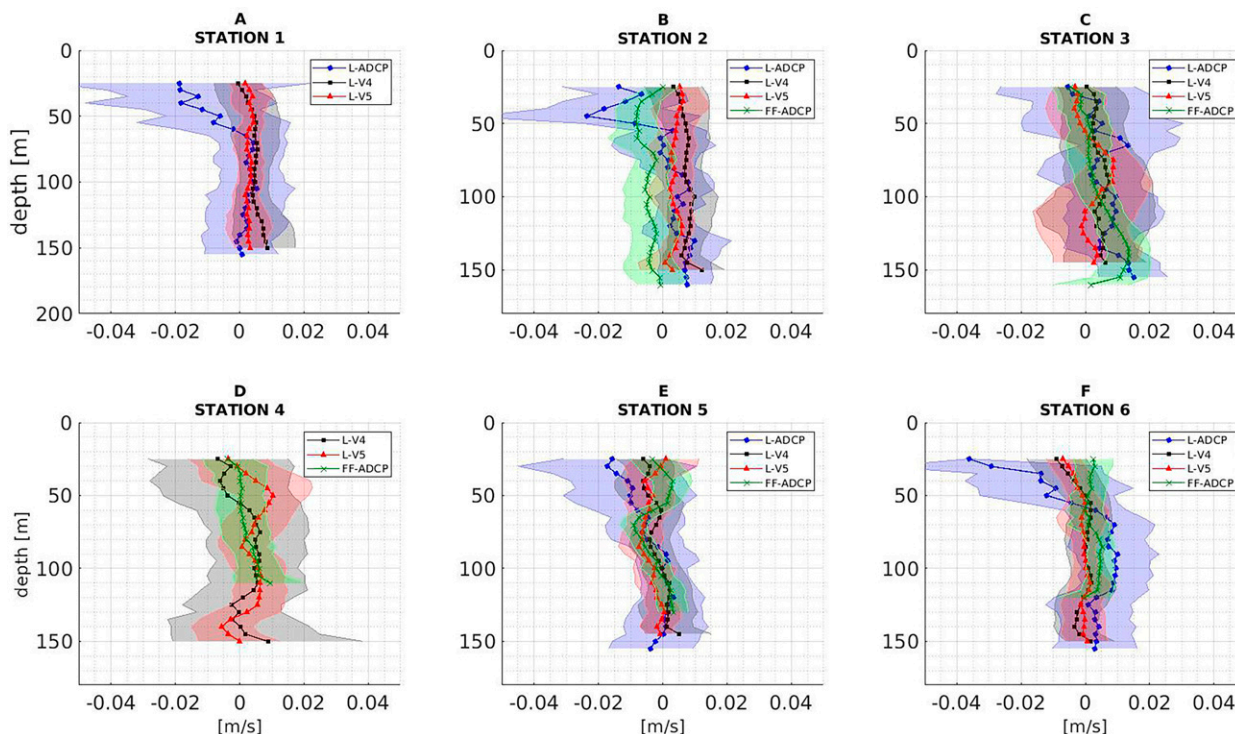


FIG. 10. Vertical velocities measured during downcast by the L-ADCP (blue), the L-V4 (black), the L-V5th (red), and the FF-ADCP (green), for stations (a) 1 to (f) 6. Means (lines and markers) and standard deviations (shaded areas) of vertical velocities are plotted as a function of depth.

Finally, the velocity estimated from the pressure measurements  $w_{\text{pkg}}$  is also a potential source of error. However, given the two extreme resolution of the pressure sensors used (0.1 and 6.8 cm respectively associated to the Sentinel V and the SBE 911, see Table 1), we estimate the propagation of such an uncertainty in the final vertical velocity profiles to be from the order of  $2 \times 10^{-4} \text{ m s}^{-1}$  for the L-V4 and L-V5th resulting profiles to  $1 \times 10^{-2} \text{ m s}^{-1}$  for the L-ADCP resulting profiles. Depending on the method used, the error in the pressure measurement may or may not represent a significant contribution to the final standard deviation.

Thus, two conclusions can be drawn:

- the main sources of error contributing to the standard deviations correspond to the tile slope one and to the pressure-derived  $w_{\text{pkg}}$  one;
- the spatiotemporal variation for each profile should not be neglected, and also contributes to the observed standard deviation.

#### 4. Discussion

The comparison of all the downcast profiles (Fig. 10) highlights a systematic good agreement in terms of both mean values and standard deviations between the two Sentinel V recordings (with the four beams—L-V4—and the fifth beam—L-V5th). In contrast, the profiles measured by the L-ADCP are more variable with depth. This vertical variability is particularly pronounced in the first 50 m of the water

column. In addition, the downcast profiles acquired, on one hand, with the new L-V5th and, on the other hand, with the FF-ADCP, are more stable over the entire sampled water column, with smaller and more homogeneous standard deviations than those obtained with the L-ADCP. Note that the higher the frequency of the acoustic pulse, the lower the uncertainty of the measurement (K. Grangier, Teledyne RDI, 2020, personal communication). As expected, the uncertainty on the Sentinel V (500 kHz) measurement is lower than the one of the L-ADCP (300 kHz).

Furthermore, Fig. 10 also shows that standard deviations of the FF-ADCP measurements are not affected by the sea state at the surface. Indeed, the standard deviation values remain stable around a few  $10^{-3} \text{ m s}^{-1}$ , even at station 4, when we had rough sea conditions.

The mean values of  $w$ , and associated standard deviations, are estimated at each station in three different layers of the water column: 25–50, 50–100, and 100–150 m deep (Fig. 11). These  $w$  mean values are on the order of magnitude of  $10^{-3} \text{ m s}^{-1}$  without a predominant trend. The greatest uncertainty in vertical velocities is contained in the upper layer (until 50 m depth), under the direct influence of weather conditions resulting in a natural variability of these velocities. Below this depth, the means and standard deviations are reduced, and the differences between the layers 50–100 and 100–150 m, for a given station and ADCP, are minor. Standard deviations show greater uncertainty depending on the measuring instrument. Then we consider vertical velocities in the water column over its entire sampled depth (i.e., 25–150 m)

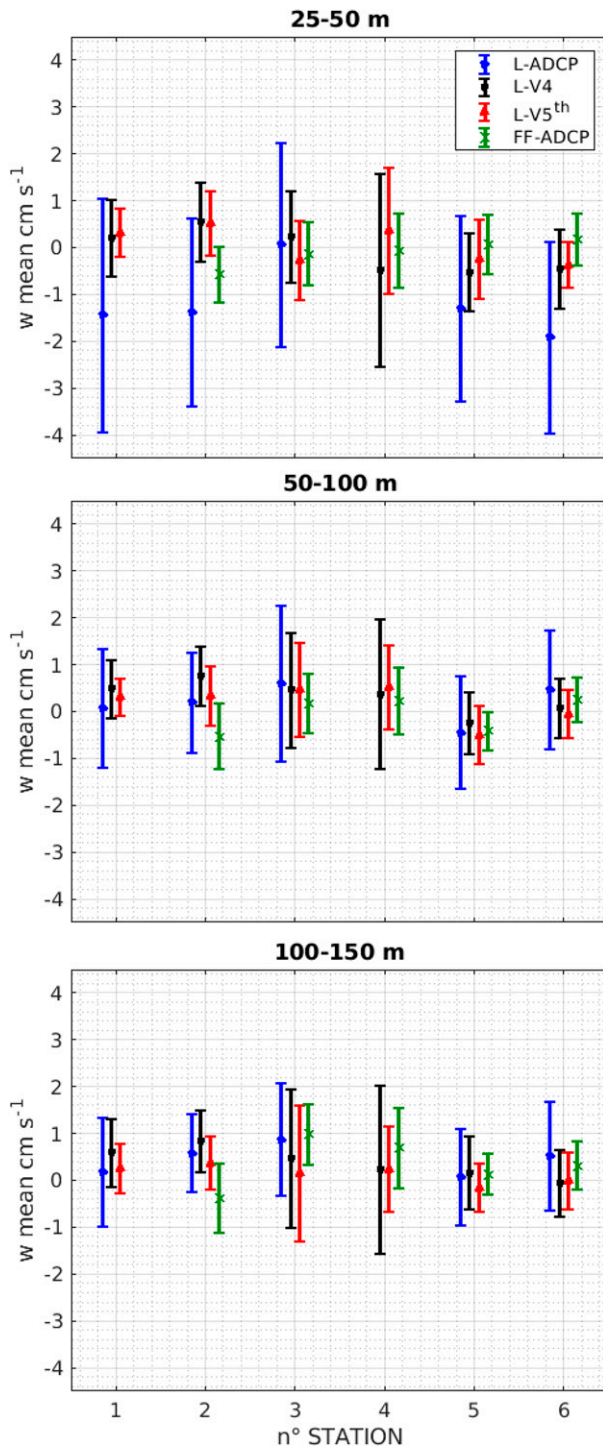


FIG. 11. Means and standard deviations of the downcast profiles of vertical velocities, averaged between three layers, (top) 25–50, (middle) 50–100, and (bottom) 100–150 m, depending on the stations, and according to the ADCP: L-ADCP (blue), L-V4 (black), L-V5th (red), and FF-ADCP (green).

and we evaluate the average standard deviation for the 2, 3, 5, and 6 stations. The orders of magnitude of these standard deviations range from  $10^{-3}$  to  $10^{-2}$   $\text{m s}^{-1}$ . They can be classified in decreasing order as follows: L-ADCP ( $=1.3 \times 10^{-2} \pm 0.2 \times 10^{-2}$   $\text{m s}^{-1}$ ), L-V4 ( $=0.9 \times 10^{-2} \pm 0.3 \times 10^{-2}$   $\text{m s}^{-1}$ ), L-V5th ( $=0.7 \times 10^{-2} \pm 0.2 \times 10^{-2}$   $\text{m s}^{-1}$ ), and FF-ADCP ( $=0.6 \times 10^{-2} \pm 0.1 \times 10^{-2}$   $\text{m s}^{-1}$ ).

We evaluate the occurrence of data acquisitions for each method dividing the vertical profiles in bins of 5 m thickness. For each type of ADCP, the occurrence is greater than or equal to 50 (without counting NaN values, obviously), and it is stable between stations for a given method. It should be noted that the free-fall sampling presents 3 times more occurrences than the measurements by the lowered method, due to its 3-times-slower free-falling speed. Nevertheless, an artificial reduction of this occurrence by using only one or two downcasts for the elaboration of the final FF-ADCP profiles (not shown), does not significantly influence the resulting standard deviation. Therefore, there is no significant error in the measurement statistics caused by data occurrence.

We know that the acoustic measurement technique, especially in the first 200 m of the water column, is likely to encounter numerous interferences and generate measurement errors. Therefore, we have taken into account the different sources of acoustic interference in this study.

First of all, the measured vertical velocity profiles are studied below 25 m depth, which makes it possible to avoid acoustic interference with the surface as well as swell and orbital current effects or divergence.

Then, an acoustic interference with the vessel mounted ADCP was observed in the FF-ADCP profiles. This interference was clearly identified in the vertical velocity time series by the linear propagation of noise over a constant thickness of two bins (10 m). Measurements showing this interference have been removed. This type of interference was not observed in the measurements from the lowered method, due to the distance between the vessel mounted ADCP and the position of the L-ADCP and the Sentinel V launched at the stern of the ship, in contrast to the FF-ADCP, launched by the side of the ship.

Finally, we investigated the speed of sound variation's potential effects on the following parameters: particle's size detection, vertical bin length estimation, and radial velocity.

The ADCPs used in this study detect particles larger than 3 mm for the Sentinel V and 4.9 mm for the two Workhorses. This detection limit slightly fluctuates in the first 200 m because the speed of sound itself is estimated between 1506 and 1514  $\text{m s}^{-1}$ , representing a variation of 0.3% over this thickness. The use of quality criteria such as correlation and echo intensity in the processing chain ensures that interferences due to mineral or organic particles, which is a potential source of significant error in the measurement, is avoided to a certain extent. Moreover, the stations were carried out in relatively clear waters and during daylight hours, thus avoiding nyctemeral migration processes, source of acoustic interference. This type of interference is apparent in the vessel mounted ADCP data (not shown) at night fall or day rise with the

migration of zooplankton such as pteropods or krill swarms (usually *Cavolinia inyexa* and *Meganctiphanes norvegica*) well-known in this region of the northwestern Mediterranean Sea (Sardou et al. 1996; Tarling et al. 1999, 2001). Finally the sound speed variation, here estimated to be  $C_{TEOS-10}/C_{ADCP} < 0.3\%$ , involves an error on the vertical bin length on the order of 1.5 cm for 5 m cells. If we consider that the mean values of L-V5th measurements vary between stations on the order of  $4 \text{ mm s}^{-1}$  (in average), its effect ( $4 \times 0.3\%$ ) on the radial velocity amounts to  $\pm 0.012 \text{ mm s}^{-1}$ . Consequently, the errors associated with the estimation of the speed of sound are largely negligible, which is why our implementation method does not require significant correction on this parameter.

## 5. Conclusions

In conclusion, we have compared four independent methods for the in situ measurement of vertical velocities in an oceanic region characterized by a low-energy circulation. We tested two different instruments (ADCP with 4 and 5 beams) and two different deployment techniques (classical rosette casts, free-fall casts). Our results show that the fifth beam of the Sentinel V provides the most precise measurement (mean values on the order of a few  $10^{-3} \text{ m s}^{-1}$  with standard deviations on the order of  $10^{-2} \text{ m s}^{-1}$ ) among those tested with the same lowered technique. Meanwhile, the free-fall sampling technique has shown the best stability in standard deviation variations between stations, with values on the order of a few  $10^{-3} \text{ m s}^{-1}$ .

The Ligurian Sea is characterized by a cyclonic general circulation pattern with a geostrophic flow along the coastal line (Esposito and Manzella 1982). Most of the sampling stations were located in this general circulation. Only stations 4 and 5 were positioned on the outer edge of the Northern Current (Millot 1999). Except for the rougher sea state conditions of station 4 driven by an intense but time limited storm event, the study area was characterized by low-energy dynamics and the cyclonic recirculation present on site remained stable throughout the cruise. Despite the limited size of our dataset, due to meteorological conditions encountered during the FUMSECK cruise, our accurate analysis of all the possible error sources allowed us to emphasize that instrumental errors have a contribution of few  $10^{-3} \text{ m s}^{-1}$  when the environmental variability in our study area is on the same order of magnitude. Indeed, in the period and region during which the FUMSECK stations took place, the oceanic circulation is characterized by a moderate coastal current and a weak cyclonic gyre. Furthermore, we show that the free-fall methodology provides better precision, in particular with rough sea conditions, by removing noise due to the anchoring to the vessel. Hence we conclude that the best methodology will be to deploy a free-falling Sentinel V.

Compared to classical studies performed in high-energy ocean (Thurnherr 2011; D'Asaro et al. 2017; Tarry et al. 2021), our work provides a method for measuring vertical velocities also applicable to a low-energy ocean, where Tzortzis et al. (2021) showed that fine-scale dynamics can have an important role in structuring the microbial community. These

low-energy ocean conditions actually represent the majority of the oceans. This new possibility of measuring low-energy vertical velocities sets the stage for more specific studies of physical–biological coupling in fine-scale structures.

Knowing that the methodology for in situ measurement of vertical velocities is ready for use, and after this first test in real conditions, it will be interesting to validate and generalize the direct acquisition of the vertical component of the oceanic current during other cruises. This will contribute to investigations in different fields: physical, biological, or biogeochemical. In the framework of the international project related to the new-generation altimetry satellite SWOT (launch planned in 2022), several cruises (JULIO-VVPTest2022 PI: J.-L. Fuda; PROTEVS 2022 PI: F. Dumas; BIOSWOT-Med 2023 PIs: A. Doglioli and G. Grégori) currently in preparation will use this method in order to obtain in situ measurement of vertical velocities in oceanic areas with fine-scale dynamics and/or at periods for which this vertical component of the current should be much more intense and contrasted. Let us recall that the interest of developing such an analytical method for direct in situ measurement of the vertical component of ocean currents is based on the growing need for information in all fields of oceanographic studies: vertical velocities playing a key role in the export of  $\text{CO}_2$  as well as organic and mineral matter.

*Acknowledgments.* We thank the captain and the crew of the R/V *Tethys II* for help in deployment of instruments. We thank Kévin Grangier for providing the Sentinel V and helpful comments. We also thank Nagib Bhairy for the postcruise processing of the CTD data, and all the members of the Service Atmosphère Mer for their punctual help. This study was initiated by the OPLC team of the Mediterranean Institute of Oceanography. Caroline Comby is now supported by a MENRT Ph.D. grant. All of this research is supported by the BioSWOT project and the FUMSECK-*vv* LEFE project.

*Data availability statement.* Supporting data cannot be made openly available at this time. As soon as all the FUMSECK papers are published, the data will be publicly available: <https://dataset.osupytheas.fr/geonetwork/srv/eng/catalog.search#/metadata/5bda8ab8-79e7-4dec-9bcb-25a3196e2f9a>.

## REFERENCES

- Allen, J. T., D. A. Smeed, A. J. G. Nurser, J. W. Zhang, and M. Rixen, 2001: Diagnosis of vertical velocities with the QG omega equation: An examination of the errors due to sampling strategy. *Deep-Sea Res. I*, **48**, 315–346, [https://doi.org/10.1016/S0967-0637\(00\)00035-2](https://doi.org/10.1016/S0967-0637(00)00035-2).
- Astraldi, M., G. P. Gasparini, G. M. R. Manzella, and T. S. Hopkins, 1990: Temporal variability of currents in the eastern Ligurian Sea. *J. Geophys. Res.*, **95**, 1515–1522, <https://doi.org/10.1029/JC095iC02p01515>.
- Barrillon, S., 2019: FUMSECK cruise report. FUMSECK Rep., 33 pp., <https://archimer.ifremer.fr/doc/00636/74854/>.
- Bower, A. S., and T. Rossby, 1989: Evidence of cross-frontal exchange processes in the Gulf Stream based in isopycnal

- RAFOS float data. *J. Phys. Oceanogr.*, **19**, 1177–1190, [https://doi.org/10.1175/1520-0485\(1989\)019<1177:EOCFEP>2.0.CO;2](https://doi.org/10.1175/1520-0485(1989)019<1177:EOCFEP>2.0.CO;2).
- Boyd, P. W., H. Claustre, M. Levy, D. A. Siegel, and T. Weber, 2019: Multi-faceted particle pumps drive carbon sequestration in the ocean. *Nature*, **568**, 327–335, <https://doi.org/10.1038/s41586-019-1098-2>.
- Canuto, V. M., and Y. Cheng, 2017: Contribution of sub-mesoscales to the vertical velocity: The  $\omega$ -equation. *Ocean Modell.*, **115**, 70–76, <https://doi.org/10.1016/j.ocemod.2017.05.004>.
- D'Asaro, E. A., and Coauthors, 2017: Ocean convergence and the dispersion of flotsam. *Proc. Natl. Acad. Sci. USA*, **115**, 1162–1167, <https://doi.org/10.1073/pnas.1718453115>.
- Doglioli, A., 2015: OSCAHR cruise, RV Téthys II. Campagnes Océanographiques Françaises, <https://campagnes.flotteoceanographique.fr/campagnes/15008800/>.
- Esposito, A., and G. Manzella, 1982: Current circulation in the Ligurian Sea. *Elsevier Oceanogr. Ser.*, **34**, 187–203, [https://doi.org/10.1016/S0422-9894\(08\)71245-5](https://doi.org/10.1016/S0422-9894(08)71245-5).
- Ferrari, R., and C. Wunsch, 2009: Ocean circulation kinetic energy: Reservoirs, sources, and sinks. *Annu. Rev. Fluid Mech.*, **41**, 253–282, <https://doi.org/10.1146/annurev.fluid.40.111406.102139>.
- Fiekas, V., H. Leach, K.-J. Mirbach, and J. D. Woods, 1994: Mesoscale instability and upwelling. Part 1: Observations at the North Atlantic Intergyre Front. *J. Phys. Oceanogr.*, **24**, 1750–1758, [https://doi.org/10.1175/1520-0485\(1994\)024<1750:MIAUPO>2.0.CO;2](https://doi.org/10.1175/1520-0485(1994)024<1750:MIAUPO>2.0.CO;2).
- Firing, E., and R. Gordon, 1990: Deep ocean acoustic Doppler current profiling. *Proc. IEEE Fourth Working Conf. on Current Measurements*, Clinton, MD, IEEE, 192–201, <https://doi.org/10.1109/CURM.1990.110905>.
- Fischer, J., and M. Visbeck, 1993: Velocity profiling with self-contained ADCPs. *J. Atmos. Oceanic Technol.*, **10**, 764–773, [https://doi.org/10.1175/1520-0426\(1993\)010<0764:DVPWSC>2.0.CO;2](https://doi.org/10.1175/1520-0426(1993)010<0764:DVPWSC>2.0.CO;2).
- Frajka-Williams, E., C. C. Eriksen, P. B. Rhines, and R. R. Harcourt, 2011: Determining vertical water velocities from Seaglider. *J. Atmos. Oceanic Technol.*, **28**, 1641–1656, <https://doi.org/10.1175/2011JTECH0830.1>.
- Fuda, J.-L., F. Marin, F. Durand, and T. Terre, 2013: Diagnosing ocean vertical velocities off New Caledonia from a SPRAY glider. *General Assembly 2013*, Vienna, Austria, EGU, 9721, <https://meetingorganizer.copernicus.org/EGU2013/EGU2013-9721.pdf>.
- Giordani, H., L. Prieur, and G. Caniaux, 2006: Advanced insights into sources of vertical velocity in the ocean. *Ocean Dyn.*, **56**, 513–524, <https://doi.org/10.1007/s10236-005-0050-1>.
- Klein, P., and G. Lapeyre, 2009: The oceanic vertical pump induced by mesoscale and submesoscale turbulence. *Annu. Rev. Mar. Sci.*, **1**, 351–375, <https://doi.org/10.1146/annurev.marine.010908.163704>.
- Lévy, M., D. Iovino, L. Resplandy, P. Klein, G. Madec, A.-M. Tréguier, S. Masson, and K. Takahashi, 2012: Large-scale impacts of submesoscale dynamics on phytoplankton: Local and remote effects. *Ocean Modell.*, **43–44**, 77–93, <https://doi.org/10.1016/j.ocemod.2011.12.003>.
- , P. J. S. Franks, and K. S. Smith, 2018: The role of submesoscale currents in structuring marine ecosystems. *Nat. Commun.*, **9**, 4758, <https://doi.org/10.1038/s41467-018-07059-3>.
- Lien, R.-C., T. Y. Tang, M. H. Chang, and E. A. D'Asaro, 2005: Energy of nonlinear internal waves in the South China Sea. *Geophys. Res. Lett.*, **32**, L05615, <https://doi.org/10.1029/2004GL020212>.
- Lindstrom, S. S., and D. P. Watts, 1994: Vertical motion in the Gulf Stream near 68°W. *J. Phys. Oceanogr.*, **24**, 2321–2333, [https://doi.org/10.1175/1520-0485\(1994\)024<2321:VMITGS>2.0.CO;2](https://doi.org/10.1175/1520-0485(1994)024<2321:VMITGS>2.0.CO;2).
- Mahadevan, A., 2016: The impact of submesoscale physics on primary productivity of plankton. *Annu. Rev. Mar. Sci.*, **8**, 161–184, <https://doi.org/10.1146/annurev-marine-010814-015912>.
- , and A. Tandon, 2006: An analysis of mechanisms for submesoscale vertical motion at ocean fronts. *Ocean Modell.*, **14**, 241–256, <https://doi.org/10.1016/j.ocemod.2006.05.006>.
- Margirier, F., A. Bosse, P. Testor, B. L'Hévéder, L. Mortier, and D. Smeed, 2017: Characterization of convective plumes associated with oceanic deep convection in the northwestern Mediterranean from high-resolution in situ data collected by gliders. *J. Geophys. Res. Oceans*, **122**, 9814–9826, <https://doi.org/10.1002/2016JC012633>.
- Martin, A. P., K. J. Richards, and M. J. R. Fasham, 2001: Phytoplankton production and community structure in an unstable frontal region. *J. Mar. Syst.*, **28**, 65–89, [https://doi.org/10.1016/S0924-7963\(00\)00084-1](https://doi.org/10.1016/S0924-7963(00)00084-1).
- McGillicuddy, D. J., 2016: Mechanisms of physical-biological-biogeochemical interaction at the oceanic mesoscale. *Annu. Rev. Mar. Sci.*, **8**, 125–159, <https://doi.org/10.1146/annurev-marine-010814-015606>.
- McWilliams, J. C., 2016: Submesoscale currents in the ocean. *Proc. Roy. Soc.*, **472A**, 20160117, <https://doi.org/10.1098/rspa.2016.0117>.
- Meloni, M., J. Bouffard, A. M. Doglioli, A. A. Petrenko, and G. Valladeau, 2019: Toward science-oriented validations of coastal altimetry: Application to the Ligurian Sea. *Remote Sens. Environ.*, **224**, 275–288, <https://doi.org/10.1016/j.rse.2019.01.028>.
- Merckelbach, L., D. Smeed, and G. Griffiths, 2010: Vertical water velocities from underwater gliders. *J. Atmos. Oceanic Technol.*, **27**, 547–563, <https://doi.org/10.1175/2009JTECH0710.1>.
- Millot, C., 1999: Circulation in the western Mediterranean Sea. *J. Mar. Syst.*, **20**, 423–442, [https://doi.org/10.1016/S0924-7963\(98\)00078-5](https://doi.org/10.1016/S0924-7963(98)00078-5).
- Petrenko, A. A., 2003: Variability of circulation features in the Gulf of Lion NW Mediterranean Sea. Importance of inertial currents. *Oceanol. Acta*, **26**, 323–338, [https://doi.org/10.1016/S0399-1784\(03\)00038-0](https://doi.org/10.1016/S0399-1784(03)00038-0).
- Pinot, J.-M., J. Tintoré, and D.-P. Wang, 1996: A study of the omega equation for diagnosing vertical motions at ocean fronts. *J. Mar. Res.*, **54**, 239–259, <https://doi.org/10.1357/002240963213358>.
- Pollard, R. T., and L. A. Regier, 1992: Vorticity and vertical circulation at an ocean front. *J. Phys. Oceanogr.*, **22**, 609–625, [https://doi.org/10.1175/1520-0485\(1992\)022<0609:VAVCAA>2.0.CO;2](https://doi.org/10.1175/1520-0485(1992)022<0609:VAVCAA>2.0.CO;2).
- Polzin, K., E. Kunze, J. Hummon, and E. Firing, 2002: The fine-scale response of lowered ADCP velocity profiles. *J. Atmos. Oceanic Technol.*, **19**, 205–224, [https://doi.org/10.1175/1520-0426\(2002\)019<0205:TFROLA>2.0.CO;2](https://doi.org/10.1175/1520-0426(2002)019<0205:TFROLA>2.0.CO;2).
- Rousselet, L., and Coauthors, 2019: Vertical motions and their effects on a biogeochemical tracer in a cyclonic structure finely observed in the Ligurian Sea. *J. Geophys. Res. Oceans*, **124**, 3561–3574, <https://doi.org/10.1029/2018JC014392>.
- Ruiz, S., and Coauthors, 2019: Effects of oceanic mesoscale and submesoscale frontal processes on the vertical transport of phytoplankton. *J. Geophys. Res. Oceans*, **124**, 5999–6014, <https://doi.org/10.1029/2019JC015034>.
- Sardou, J., M. Etienne, and V. Andersen, 1996: Seasonal abundance and vertical distributions of macroplankton and

- micronekton in the northwestern Mediterranean Sea. *Oceanol. Acta.*, **19**, 645–656.
- Sasaki, H., P. Klein, B. Qiu, and Y. Sasai, 2014: Impact of oceanic-scale interactions on the seasonal modulation of ocean dynamics by the atmosphere. *Nat. Commun.*, **5**, 5636, <https://doi.org/10.1038/ncomms6636>.
- Schott, F., and K. D. Leaman, 1991: Observations with moored acoustic Doppler current profilers in the convection regime in the Golfe du Lion. *J. Phys. Oceanogr.*, **21**, 558–574, [https://doi.org/10.1175/1520-0485\(1991\)021<0558:OWMADC>2.0.CO;2](https://doi.org/10.1175/1520-0485(1991)021<0558:OWMADC>2.0.CO;2).
- , M. Visbeck, U. Send, J. Fischer, L. Stramma, and Y. Desaubies, 1996: Observations of deep convection in the Gulf of Lions, northern Mediterranean during the winter of 1991/92. *J. Phys. Oceanogr.*, **26**, 505–524, [https://doi.org/10.1175/1520-0485\(1996\)026<0505:OODCIT>2.0.CO;2](https://doi.org/10.1175/1520-0485(1996)026<0505:OODCIT>2.0.CO;2).
- Shearman, R. K., J. A. Barth, and P. M. Kosro, 1999: Diagnosis of the three-dimensional circulation associated with mesoscale motion in the California Current. *J. Phys. Oceanogr.*, **29**, 651–670, [https://doi.org/10.1175/1520-0485\(1999\)029<0651:DOTTDC>2.0.CO;2](https://doi.org/10.1175/1520-0485(1999)029<0651:DOTTDC>2.0.CO;2).
- Steffen, E. L., and E. A. D'Asaro, 2002: Deep convection in the Labrador Sea as observed by Lagrangian floats. *J. Phys. Oceanogr.*, **32**, 475–492, [https://doi.org/10.1175/1520-0485\(2002\)032<0475:DCITLS>2.0.CO;2](https://doi.org/10.1175/1520-0485(2002)032<0475:DCITLS>2.0.CO;2).
- Strass, V. H., 1994: Mesoscale instability and upwelling. Part 2: Testing the diagnostics of vertical motion with a three-dimensional ocean front model. *J. Phys. Oceanogr.*, **24**, 1759–1767, [https://doi.org/10.1175/1520-0485\(1994\)024<1759:MIAUPT>2.0.CO;2](https://doi.org/10.1175/1520-0485(1994)024<1759:MIAUPT>2.0.CO;2).
- Tarling, G. A., F. Buchholz, and J. B. L. Matthews, 1999: The effect of a lunar eclipse on the vertical migration behaviour of *Meganyctiphanes norvegica* (crustacea: Euphausiacea) in the Ligurian sea. *J. Plankton Res.*, **21**, 1475–1488, <https://doi.org/10.1093/plankt/21.8.1475>.
- , J. B. L. Matthews, P. David, O. Guerin, and F. Buchholz, 2001: The swarm dynamics of northern krill (*Meganyctiphanes norvegica*) and pteropods (*Cavolinia inflexa*) during vertical migration in the Ligurian Sea observed by an acoustic Doppler current profiler. *Deep-Sea Res. I*, **48**, 1671–1686, [https://doi.org/10.1016/S0967-0637\(00\)00105-9](https://doi.org/10.1016/S0967-0637(00)00105-9).
- Tarry, D. R., and Coauthors, 2021: Frontal convergence and vertical velocity measured by drifters in the Alboran Sea. *J. Geophys. Res. Oceans*, **126**, e2020JC016614, <https://doi.org/10.1029/2020JC016614>.
- Thomas, L., A. Tandon, and A. Mahadevan, 2008: Submesoscale processes and dynamics. *Ocean Modeling in an Eddy Regime*, *Geophys. Monogr.*, Vol. 177, Amer. Geophys. Union, 17–38, <https://doi.org/10.1029/177GM04>.
- Thurnherr, A. M., 2011: Vertical velocity from LADCP data. *IEEE/OES 10th Current, Waves and Turbulence Measurements*, Monterey, CA, IEEE, 198–204, <https://doi.org/10.1109/CWTM.2011.5759552>.
- Tintoré, J., D. Gomis, S. Alonso, and G. Parrilla, 1991: Mesoscale dynamics and vertical motion in the Alboran Sea. *J. Phys. Oceanogr.*, **21**, 811–823, [https://doi.org/10.1175/1520-0485\(1991\)021<0811:MDAVMI>2.0.CO;2](https://doi.org/10.1175/1520-0485(1991)021<0811:MDAVMI>2.0.CO;2).
- Tzortzis, R., and Coauthors, 2021: Impact of moderately energetic fine-scale dynamics on the phytoplankton community structure in the western Mediterranean Sea. *Biogeosciences*, **18**, 6455–6477, <https://doi.org/10.5194/bg-18-6455-2021>.
- Weller, R. A., D. L. Rudnick, N. J. Pennington, R. P. Trask, and J. R. Valdes, 1990: Measuring upper ocean variability from an array of surface moorings in the subtropical convergence zone. *J. Atmos. Oceanic Technol.*, **7**, 68–84, [https://doi.org/10.1175/1520-0426\(1990\)007<0068:MUOVFA>2.0.CO;2](https://doi.org/10.1175/1520-0426(1990)007<0068:MUOVFA>2.0.CO;2).
- Yu, X., A. C. Naveira Garabato, A. P. Martin, C. E. Buckingham, L. Brannigan, and Z. Su, 2019: An annual cycle of submesoscale vertical flow and restratification in the upper ocean. *J. Phys. Oceanogr.*, **49**, 1439–1461, <https://doi.org/10.1175/JPO-D-18-0253.1>.